Structural Design of a MAME UAV Wing using High-Fidelity Numerical Tools

Vítor Manuel Tavares Silva
vitortavaressilva8@tecnico.ulisboa.pt

Instituto Superior Técnico, Universidade de Lisboa, Portugal

December 2023

Abstract

With the rapid growth of the UAV market, more efficient solutions give a huge competitive advantage for manufacturers. With optimisation techniques and high-fidelity analyses in aircraft design, it is possible to develop better solutions. This work addresses the desire of a leading UAV manufacturer to improve its fleet to remain competitive in the surveillance UAV market. For this, a structural analysis tool using the finite element method was demonstrated, which was then used as part of a structural optimisation framework. For this demonstration, static analyses of the wingbox of an existing UAV model, with a CFRP material with different lay-ups were carried out for cruise and 4g load cases. Results of deformation and failure helped to evaluate the wingbox structural behaviour. Validation of the numerical design framework using available experimental data presented slight differences due to model simplifications and lack of accurate material properties. Seven new optimal wingbox solutions were found with variable ply thicknesses and fibre orientations. The first was optimised only with failure constraints; a maximum allowed displacement was added to the following two but had different starting solutions; manufacturing constraints such as ply angle continuity, orthogonality of plies and monotonically decreasing thickness were added to the next three, respectively; and finally, for the fully constrained solution, a maximum allowed wing tip torsion was added. To check for possible local minima, this last optimisation problem was evaluated again with a different baseline. Mass reduction between about 44% and 56%, while respecting a safety factor of 1.5, was found possible.
Keywords: optimisation, design framework, adjoint method, finite element method, composite materials, fibre orientation

1. Introduction

With the continuous development and technological improvements of the Unmanned Aerial Vehicles (UAV) industry, different sizes and configurations were found useful to cover a wide range of missions. Nowadays, these vehicles are equipped with various electronic equipment, such as different cameras and sensors, depending on their intended purpose, and turning these in highly complex systems. Some use cases of these Unmanned Aerial Systems (UAS) include: inspection of photovoltaic plants, to reduce the time of manual inspections [1]; precision agriculture, for weed mapping and management, vegetation health and growth monitoring, irrigation management and crops spraying [2]; urban environment and management, to give real-time monitoring of traffic, road conditions as well as building observation [3]; disaster hazard and rescue, to quickly and accurately respond when necessary as well as post-disaster assessment and emergency response in remote places; and maritime monitoring, to control oil spills, gas pipes, whales and marine life, tracking fishing boats as well as controlling illegal immigration.

Investments in the UAS industry have been a trend to explore new and original applications. Since 2000, more than 300 start-ups entered the UAS market, focusing on hardware, support services and operations [4]. They have gathered more than 3 billion USD to develop the industry with new applications.

In order to remain competitive in this growing market, the demand for highly efficient and optimised UASs increases.

2. Tekever AR5 UAS

Tekever is a company founded in 2001 that manufactures and operates their UAS mainly for surveillance missions. An objective was set to optimise their most advanced Medium Altitude Medium Endurance (MAME) UAS - the AR5 (Fig. 1) - using high-fidelity tools. This work is the starting point of this project, introducing the numerical tools and proving the concept.

Figure 1: Tekever AR5

The main AR5 specifications are resumed in Tab. 1.

Table 1: Some characteristics of the Tekever's AR5 [5]

Wing span	Cruise speed	MTOW	Payload capacity	Endurance	Communications range
7.3 m	100 km h^{-1}	180 kg	50 kg	12 h*	Unlimited (SATCOM)

* Expected endurance with inflating raft

3. Structural Analysis and Optimisation

3.1. Finite Element Method

For the structural analysis presented in this paper, the FEM method is used due to its high capabilities of modelling complex geometries and its high use in the aeronautic industry for structural applications.

For thin structures, like the wing's skin, 2D shell elements are used to model the middle plane of the skin [6]. In this work, the elements used in the analysis are the 4-node quadrangular elements based on a Mixed-Interpolation of Tensorial Components (MITC) approach, which avoid shear and membrane locking [7, 8]. For these elements, the basis theory is the classical first order deformation theory [8]. Then, with laminate constitutive equations, the stresses are obtained from the strains.

3.2. Material Characterisation and Modelling

The structures to be analysed are composed of Carbon Fibre Reinforced Polymer (CFRP) plies that, when stacked, form the laminate. Since each ply is composed of unidirectional fibres in a matrix medium, it presents an orthotropic behaviour.

To model the composite material that composes the wingbox, a smeared approach is used [9]. This method describes the composite structure using fractions of plies (f_{θ_i}) and their respective angles (θ_i) It is necessary to provide the elastic and strength properties of each ply as well as the total thickness of the laminate. With these, the global stiffness matrix is weighted with each ply fraction of a certain orientation. A visual diagram of the geometric parameters necessary for this model is presented in Fig. 2.

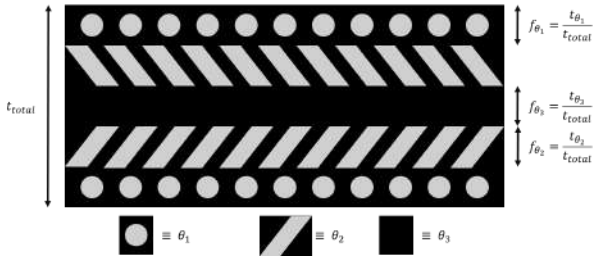

Figure 2: Composite representation with the necessary parameters to define the smeared model

To predict failure of composite materials, it is necessary to characterize the composite strength for different load conditions (axial, transverse and shear tensile stresses), which are reflected in their longitudinal, transverse and shear tensile strength parameters. In this work, the *Tsai-Wu* Criterion is used,

$$F_{TW} = F_1\sigma_1 + F_2\sigma_2 + F_{11}\sigma_1^2 + 2F_{12}\sigma_1\sigma_2 + F_{22}\sigma_2^2 + F_{66}\sigma_{12}^2 \ , \quad (1)$$

where σ_i is the stress component in the ith direction in the principal material coordinates of each ply (1 to 3 are normal stresses and 4 to 6 shear stresses) and F_{ij} are coefficients depending on the material normal and shear strengths [8]. When this F_{TW} failure index is equal or above 1, material failure is expected.

3.3. Optimisation Techniques

The general structural optimisation problem can be stated as

$$\begin{aligned} \text{minimize} \quad & f(v, u_1, ..., u_{n_l}) \\ \text{w.r.t.} \quad & v, u_1, ..., u_{n_l} \ , \\ \text{governed by} \quad & R_i(X^N(v_G), v_M, u_i) = 0 \, , \\ \text{subject to} \quad & g_i(v, u_i) \leq 1 \end{aligned} \quad (2)$$

where $f(v, u_1, ..., u_{n_l})$ is the objective function, $g_i(v, u_i)$ is a constraint vector for the ith load case, up to a total of n_l, $x = (v_G, v_M)$ are the design variables, divided as geometric and material design variables, respectively, $X^N(v_G)$ are the nodal locations, u_i are the state variables for the ith load case and R_i are the finite-element residuals.

In the context of this work, the gradient-based optimisation seems the most favourable approach since the number of design variables is high and the functions of interest are smooth. One of the most commonly used approaches to solve the optimisation problem is recurring to a sequential quadratic programming method. One great example is the

Sequential Least Squares Quadratic Programming method (SLSQP) which uses the Han–Powell quasi-Newton method with a BFGS update of the B-matrix and an L1-test function in the step-length algorithm [10]. A study [11] showed that, for a multi-dimensional Rosenbrock function, the SLSQP algorithm performed the best among several other gradient-based and -free methods, converging the fastest, with the least amount of function evaluations when obtaining the minimum C_D when changing the wing twist or shape. This result was especially good using the adjoint method for the derivatives. This SLSQP method is commonly used in aerodynamic shape optimisation [12, 13], airfoil shape optimisation problems [14] as well as aerostructural problems [15].

3.3.1 Adjoint Method

To compute gradients, either of the objective function or the constraint functions with respect to the design variables, the chosen method to make them more efficient to compute. Kennedy & Martins [16] and Kenway et al. [17], for example, used a gradient-based algorithm for an aerostructural optimisation of a wing and a wide-body transport aircraft, respectively, due to the large number of design variables (thousands), which is bigger than the number of constraints' functions. On the other hand, if the situation was the opposite, the direct method used by Werter & De Breuker [18] to minimize a wing weight with respect to some lamination parameters and the laminate thickness, would be the most efficient. One of the other key aspects, besides the use of the direct method in this case, was the use of analytically obtained sensitivities of the objective and constraints' functions with respect to the design variables that help gradient-based optimisations to be faster.

3.4. CSM Analyses' Steps and TACS Framework

From the CAD file containing the geometry information of the wingbox to be evaluated up to the output results of the finite element analysis, and the posterior optimisation, a sequence of steps need to be followed and different software used, as presented in Fig. 3, with highlight in yellow of the structural analysis components.

The CSM software used is TACS [7], an open-source FEM solver. In TACS, load cases are set to condition the problem before it is solved and boundary conditions imported from the mesh definition file. In every problem iteration, the TACS software gives function values and gradients to a gradient-based optimiser, which then iterates until the optimum solution for the intended problem is found. A flow chart representing the TACS workflow is also presented in Fig. 3.

For the optimisation process to be successful and comply with Tekever's requirements, manufacturing constraints are necessary so that the line of production and the manufacturing techniques used remain the same, while the parts themselves are optimised. To achieve this, some constraints had to be developed and incorporated into TACS. These are the orthogonal plies, the monotonic thickness and the wing tip torsion. Using a plate test case, these constraints' implementation was validated.

4. Teveker AR5 Wing Structural Analysis

4.1. AR5 Wing Definition

The baseline and start of the optimisation process of the AR5 is its wing, since it is the main component of the UAV. A simplified and more detailed version of the internal wingbox structure are represented in Fig. 4.

The wingbox can be parametrised in several ways. To do this, some groups within the structure are created, sharing the same parameters, to later, in the optimisation process, these varying equally within the group. In Fig. 5, the groups can be observed in different colours as well as the internal wingbox structure and reference frame used throughout its analysis. The parameters that define each group are total thickness, type of material, their proportions and the ply angles (parameters from Fig. 2).

4.2. Wingbox Material Definition

The AR5 wingbox is composed of sandwich composite components with different thicknesses and fractions of core and shell material. A representation of these sandwich components is shown in Fig. 6.

The core consists on a low weight rigid foam which gives the necessary stiffness to the wing, with a very low weight. Different versions and proportions of this core are used depending on the wingbox section. The physical and mechanical properties used are summarized in Tab. 2. Since the foam core properties in-plane are independent of direction, this material can be modelled as isotropic.

Table 2: Foam core properties

Density
Tensile modulus in the plane
Shear modulus
Tensile strength in the plane

For the shell, a CFRP layup is used with plies of 0° and 90° as a starting point. A summary of the properties obtained can be seen in Tab. 3.

To define the material composed of both the foam and CFRP, present in the wingbox, the constitutive model explained in Sec. 3.2 is used.

Finally, to acknowledge the possible differences

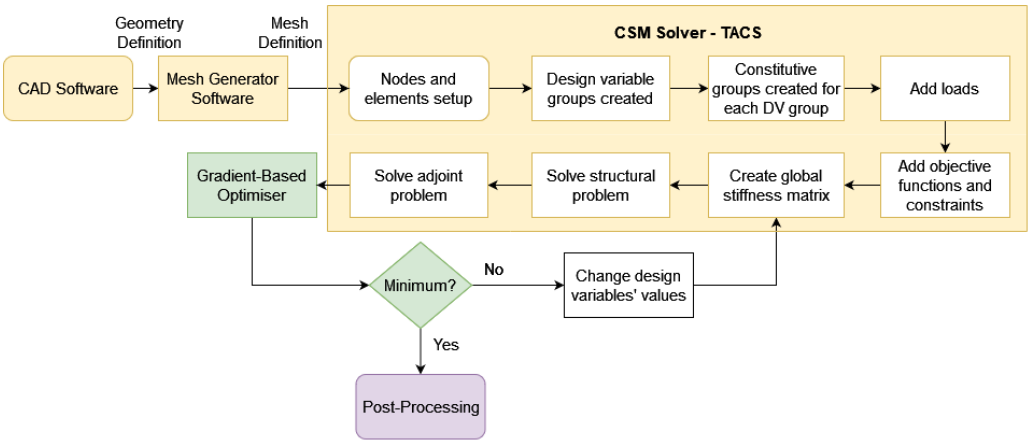

Figure 3: Flow chart of the steps to solve an optimisation problem

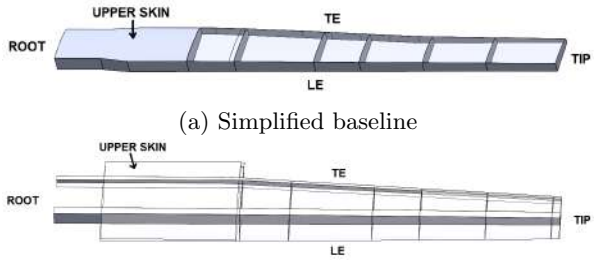

(a) Simplified baseline

(b) Detailed model

Figure 4: Wingbox structure of Tekever AR5

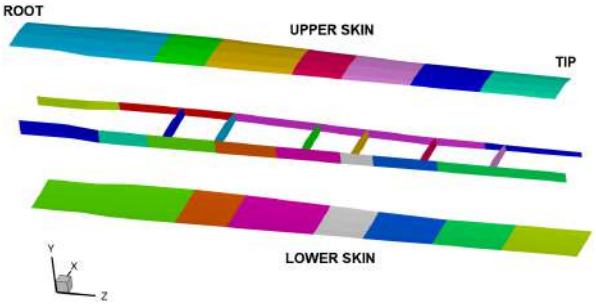

Figure 5: Representation of the design variable groups on the simpler wingbox

Table 3: Density and physical properties of CFRP ply

Density*
Young's modulus (fibre direction)*
Young's modulus (Transverse direction)*
Shear modulus
Poisson ratio
Tensile strength (fibre direction)
Compressive strength (fibre direction)
Tensile and compressive strength (transverse direction)
Shear strength

* Obtained from rule of mixtures

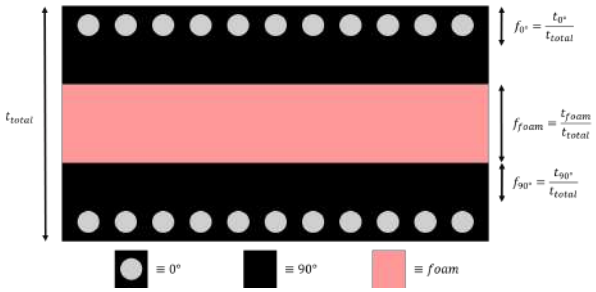

Figure 6: Representation of the sandwich composite (CFRP with black matrix and grey fibres and Airex foam in pink)

between the mass calculated from the structural model and the real mass of each component, measured by Tekever's quality control team, the error of the model relative to the measured values is given in Tab. 4.

Table 4: Error of model mass relative to measured mass of AR5 wingbox components

	Lower Skin	Upper Skin	Spars	Ribs	Total
Simpler model [%]	+19.1*	+26.1*	−30.9	−50.0	−1.7
Detailed model [%]	−33.4	−23.9	+53.5	−33.5	+1.6

* Extrapolated value

It is possible to observe that the calculated total mass is slightly underestimated in the simpler model. Firstly, for the skin mass, an extrapolation was needed to compare the real and model values since due to the simplifications needed for the wingbox meshing, the skin panels that are computed are only present between the spars. Therefore, with those panel's mass, an extrapolation was made to obtain the estimated weight of the real model skin, shown in Tab. 4. For the detailed mesh, this extrapolation was not necessary since all skin panels were considered. Nonetheless, there were still 33.4% and 23.9% less mass than in the measured lower and

upper skin, respectively, since there are a few geometric differences, specially in the simpler model, as well as material properties' differences in both. Finally, it is important to note that, overall, the total mass difference is negligible (about 2% error for both cases) and does not affect the wing's rigidity directly.

4.3. Mesh Generation and Refinement Study

The simpler structure is composed by 6 ribs, 2 spars and the skin panels between these. The simplifications include the trimming of the ribs' leading edge at the front spar, the addition of a rear spar section close to the tip and the skin panels are only present between the spars (no leading or trailing edge skin panels), as seen in Fig. 4a).

Considering that the structural model is solved in each optimisation step, it is important to choose an efficient mesh to compute the most accurate results in the least time possible and using the least amount of computational resources. To make this decision, a mesh refinement study was initially carried out for the simplified wingbox with 5 refinement levels. Firstly, using 4-node quadrangular MITC shell elements. Afterwards, higher order elements were employed.

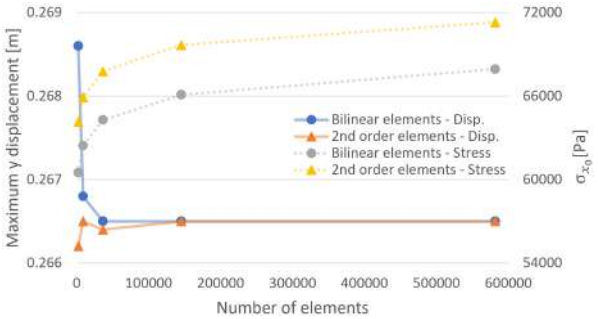

Figure 7: Mid-plane stress (σ_x^0) at root and maximum y displacement at the tip for each mesh and element type

Observing Fig. 7, it is possible to conclude that both the stress and maximum displacement converge with increasing number of elements in the mesh. The criteria to chose the final mesh was: it had to be converged and it should be the one that takes the least time and memory to solve. It was concluded that mesh 4 with bilinear elements or mesh 3 with 2^{nd} elements met these criteria. The computational cost between these two meshes is similar. However, the convergence behaviour is different since the difference between stress results of the bilinear meshes behaved monotonically decreasing while the 2^{nd} order ones did not. Additionally, the stress values are higher using the 2^{nd}. Considering that the point monitored has stress concentrations as previously mentioned, this could lead to oversized final optimal solutions. Therefore, this mesh was rejected and the next most efficient choice was mesh 4 with $145,408$ bilinear elements.

Following this study, a comparison between the detailed and simpler wingbox results was made. The element size from this study's choice was translated to the other mesh. This resulted in a mesh with $212,589$ elements and $200,312$ nodes.

4.4. Design Framework Validation

To validate the numerical design framework, experimental data was used from a static wing bending test provided by Tekever. Weights were added in the lower skin with the wing upside down and the tip displacement measured. Analysing with TACS, the maximum deflection obtained was about 0.17 m across the tip. The undeformed and deformed shapes can be observed in Fig. 8.

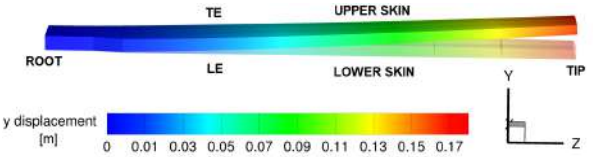

Figure 8: Wingbox's displacement in vertical direction under fixed loads

According to the ground test, the measured displacements at the tip, for the leading edge and trailing edge, were 0.12 m and 0.17 m, respectively. The fact that there is no significant difference between the leading and trailing edge from the computational results is due to a portion of the rear spar, close to the tip, not existing in reality, so the trailing edge has lower stiffness and a higher displacement in bending. Finally, the computational results reproduce overall a higher displacement and this is the expected behaviour since, with the geometry approximations, some wing elements were not added, making the wing less stiff and exhibit a larger deformation.

After this, a more detailed geometry was used to test the analysis framework capabilities. Considering that this model has more sections, such as other skin panels, the stiffness increased in comparison to the simplified wingbox.

4.5. Analysis of Cruise and 4g Manoeuvre

A comparison between the simpler and detailed model is performed using the cruise and 4.0g load conditions, to chose the most adequate mesh for the optimisations. The maximum values of failure and displacement were found present in the 4.0g condition and the results are shown in Fig. 9.

The results obtained are satisfactory and well bellow the unity for both cases, with values of 0.47 and 0.31 for the simple and detailed mesh, respectively.

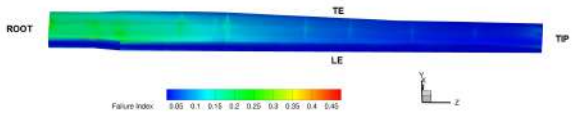

(a) Simpler wingbox's (leading edge and upper skin)

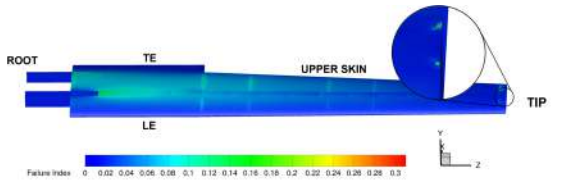

(b) Detailed wingbox's (leading edge and upper skin)

Figure 9: Failure index distribution for 4.0g condition

Consequently, this gives the structure a safety factor between 2.1 and 3.2.

Regarding the normalized vertical displacements, the maximum deflection obtained is for the 4.0g load condition with the simpler mesh, at the tip, and corresponds to about 8% of half span (0.266 m). This value indicates that the deflection is not too large relative to the wing size and it is acceptable.

4.6. Summary and Discussion of Results

A compilation of all analysis is given in Tab. 5.

Table 5: Key results across the different loads and geometries

Load Case	Model	Maximum deflection [m]	Maximum failure index	Tip rotation ($\Delta\gamma$)
Wing Bending Test	Simple	0.176	0.24	$-1.4°$
	Detailed	0.054	0.09	$-0.17°$
Cruise	Simple	0.068	0.08	$-0.12°$
	Detailed	0.029	0.06	$-0.22°$
4.0g	Simple	0.266	0.47	$-0.47°$
	Detailed	0.116	0.31	$-0.87°$

The maximum deflection results are located at the trailing edge of the wing tip. These are within a normal range of values and are not high, since the maximum is around 8% the half-span. Considering that the wing is not expected to deform too much, non-linear analyses would unnecessarily increase the computational cost so these analyses and the following optimisations are only linear.

As previously discussed, the maximum failure indexes give acceptable safety factors that indicate some room for improvement in this geometry.

Regarding the tip rotation values between the non-deformed and the deformed configuration ($\Delta\gamma$ - Fig. 13), the negative value indicates a pitch down rotation, meaning that all situations lead to a counter-acting movement to a possible divergent behaviour of the wing, which is desirable. Quantitatively, since there is no spar near the tip of the wing in the actual Tekever AR5, these values might change slightly from the ones of the simpler mesh. However, it is possible to see that this advantageous behaviour is increased with increasing load (comparing cruise to the 4.0g load condition). The outlier here is the wing bending test, that shows a much larger rotation than the other cases for the simpler mesh and the lowest rotation for the detailed mesh. For the simpler mesh, the reasoning for this behaviour is that, since the loads used are constant along the chord, which is not the case of the lift distribution, higher loads are found near the trailing edge in this test, making a higher pitch-down deflection on the wing (this is because the loads are applied in the lower skin as explained in Sec. 5.2.3). The low value in the detailed mesh is probably due to the higher rigidity of this more complete model.

The CPU and RAM was also monitored and the detailed mesh takes 9% more time and needs 57% more RAM than the simpler mesh in the 4.0g load condition. This increase in cost makes it more efficient for the optimisation to use the simpler mesh considering that those 9% more seconds scale with the number of iterations in an optimisation.

5. Tekever AR5 Wing Structural Optimisation

5.1. Problem Formulation

Tekever's goal is to minimize the structural mass and increase the efficiency of the AR5, meaning that the objective function to this problem is the total wingbox mass. This includes the ribs, spars and upper and lower skins.

$$m_{\text{total}} = m_{\text{ribs}} + m_{\text{spars}} + m_{\text{upper skin}} + m_{\text{lower skin}} \quad (3)$$

To control this mass, the variables allowed are some of the parameters that describe the wingbox design variable (DV) groups. In this case, the ones chosen are the thickness (t_i) of the ith DV group and the orientation (θ_{ij}) of the jth CFRP ply from the ith DV group.

The boundaries for each DV group are defined as: minimum of 1 mm for both skins and spar areas with foam core and 0.25 mm for the spars sections that are only constituted by CFRP; to give more freedom to the optimiser to possibly reinforce certain areas of the wingbox, a maximum of 100 mm was set. The ply angles have a lower bound of $-90°$ and a upper bound of $90°$.

Some inequality constraints are set: failure constraint, using the KS function, to make sure the failure index given in Sec. 3.2 by the Tsai-Wu criterion is limited to a maximum of 1 and ensure that the wing can withstand the loads; displacement constraint, also using the KS function, to make sure the vertical displacement stays below 12% of the half wing span; adjacency constraints, to keep a thickness difference ($|t_i - t_k|$) between a certain ith DV

group and its adjacent groups (kth DV groups) under a $\Delta_{\max}$; decreasing thickness constraint, from the root to the tip ($t_j - t_{j+1} \geq 0$), where t_j is the thickness of th jth DV group and t_{j+1} of the following (the higher the index, the closer to the root the DV group is); ply angle continuity ($\theta_{1_i} = \theta_{1_k}$ and $\theta_{2_i} = \theta_{2_k}$, where θ_{1_i} corresponds to the angle of the first ply of the $i$the DV group and k is its adjacent) to ensure the wing can be manufactured by normal methods; orthogonality between plies ($|\theta_1 - \theta_2| = 90°$) to allow the use of carbon fibre cloths with weaving pattern; and finally a maximum torsion for the wing tip ($\gamma \leq \gamma_{\max}$).

With this in mind, the fully constrained optimisation problem for this wingbox structure can be formulated as

$$
\begin{aligned}
\text{minimize} \quad & m_{\text{total}} \\
\text{w.r.t.} \quad & t_i \\
& \theta_{ij}\,, \\
\text{subject to} \quad & \text{KS(failure)} \leq 1 \\
& \text{KS(displacement)} \leq 0.12 \\
& |t_i - t_k| \leq \Delta_{max} \\
& t_j - t_{j+1} \geq 0 \\
& \theta_{1_i} = \theta_{1_k} \\
& \theta_{2_i} = \theta_{1_k} \\
& |\theta_1 - \theta_2| = 90° \\
& \gamma \leq \gamma_{\max}\,.
\end{aligned}
\tag{4}
$$

5.2. Baseline Optimisation - Case 1

For the first baseline case, only failure constraints are considered. For this and the following cases, the stopping criterion was the convergence accuracy, upon reaching the value of 10^{-6}. The history of the mass and constraints throughout the optimisation is presented in Fig. 10 to show the converging behaviour of the objective function.

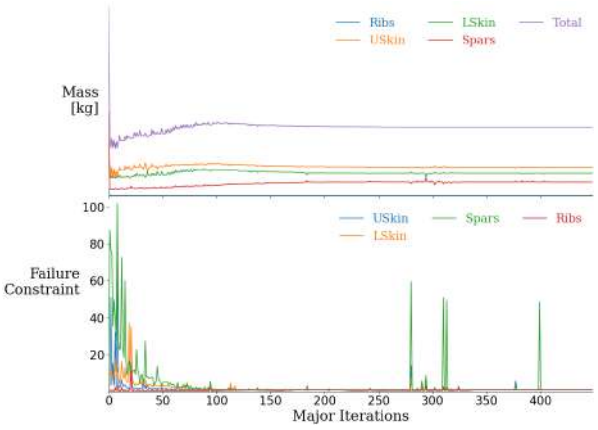

Figure 10: Objective function and failure constraint optimisation history

The optimal solution in this case resulted in overall thinner sections through all components of the wingbox. With the thinning of these and without buckling constraints present in this optimisation, it is expected that the wing displacement increases. In fact, the optimised wingbox, for this 4.0g load condition, presents a relative maximum vertical displacement of 0.18 (+126% than the baseline).

5.3. Baseline Optimisation with Displacement Constraint - Case 2

To prevent such a large displacement, another KS function, aggregating all displacements from a specific wingbox components is used, in order to more easily control the maximum displacement of that specific component.

A comparison view of the vertical displacement between this new optimal solution, the previous one and the baseline is given in Fig. 11.

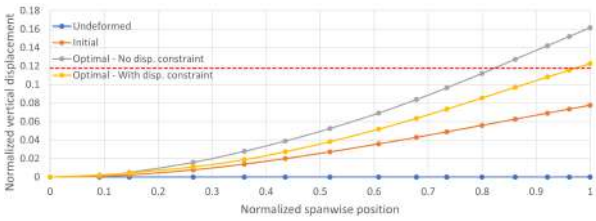

Figure 11: Front spar y deflection under 4.0g

To ensure this new constraint was respected, the thickness of the components from the previous optimal solution and the newer one increased, particularly near the root, for both the upper and lower skins. In contrast, there is a reduction in thickness near the root for both spars. This indicates that the root skin panels of the skin are more effective at increasing the wing bending stiffness and reducing the maximum displacement and it is possible to mitigate the mass gain by thinning the spars. Although making the spars thinner supposedly decreases their rigidity, the gain from the skin panels is greater and the overall mass is reduced.

Using the optimal solution obtained from the baseline optimisation as the starting point in a new optimisation with displacement constraint (Case 2 - new baseline) leads to a new solution, which corresponds to a different local minimum.

5.4. Manufacturing Constraints - Cases 3, 4 and 5

For each of these tree cases, new manufacturing constraints where necessary. In case 3, adjacency constraints to keep adjacent panels of each component with the same orientation, were applied. Although, the constraint was satisfied in the optimal solution, the plies had no relation between them, requiring the use of unidirectional fibres to build the layup.

To use woven CFRP fabric with a weave pattern, an orthogonality constraint is applied for the plies in the same DV group. Once again, another

satisfactory optimal solution was found. However, the thickness across the components was not monotonic, as Fig. 12 shows.

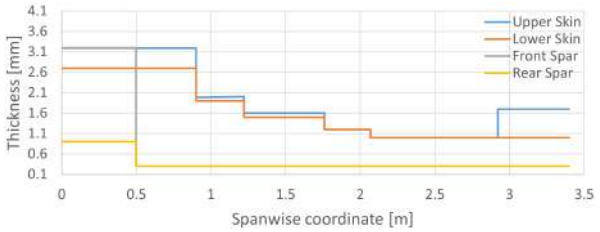

Figure 12: Thickness distribution for each component with added orthogonal plies constraint (case 4)

To make sure the spar and skin panels have a monotonic thickness, decreasing from the root to the tip, another constraint was added. This resulted in a optimal solution that could be manufactured and respected both the maximum displacement and failure index. Nonetheless, the tip torsion (γ) that this optimal solution presented, when under the 4g load, was 5.9° ($\Delta\gamma$ of 2.4° relative to the undeformed wingbox - Fig. 13). Not only this $\Delta\gamma$ is now positive (tip up) but also the absolute value of γ increased. This indicates that, the divergence behaviour is becoming a threat for the wing structure since the optimal solution is allowing a wash-in deformation under loading.

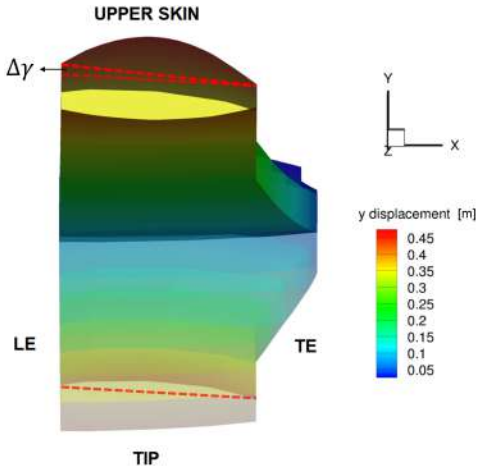

Figure 13: Tip rotation representation

5.5. Tip Torsion Constraint - Case 6

To limit this, the final added constraint to the problem was an upper limit for the tip torsion. A new optimisation problem was set up to reduce about 20% of the tip torsion, compared to the case 5 solution.

This effective reduction in torsion can be seen with the change in ply angles from case 5 (without the torsion constraint) to case 6 (with the addition of this constraint). The only components with changes are the upper skin and rear spar. Starting by the most noticeable, the rear spar, from case 5 to case 6, the fibres orientation change about 12° due to the maximum failure index being located in this component. This makes the θ_1 and θ_2 angles more perpendicular and parallel, respectively, to the displacement. In this configuration, the fibres will withstand an higher amount of load in tension and compression. This angle change has larger impact on the thicker section of the rear spar, which is exactly where the maximum failure index occurs.

Table 6: Ply angles for each component in case 5/case 6

	Upper Skin	Lower Skin	Front Spar	Rear Spar
θ_1	88.8°/87.5°	90.0°/90.0°	87.4°/87.4°	66.4°/78.8°
θ_2	−1.2°/−2.5°	0.0°/0.1°	−2.6°/−2.6°	−23.6°/−11.1°

The other difference is in the upper skin. Although it might be small, by decreasing the angle, the torsional rigidity of the skin increases (increasing the angle up to 45°). With this, the overall tip torsion decreases up to the desired value.

Since this is the last and most complete optimisation, the final failure index distribution is presented in Fig. 14 with a maximum reaching 0.87. This gives a final safety factor of 1.15 for the optimal solution. It must be noted that, once again, the point of maximum value is a stress singularity. That value only appears at that location and, further away, the highest failure indexes are about 0.4.

Similarly to case 2, since this is the last and most complete optimisation, another fully constrained problem was solved using the optimal solution from case 5 as a new starting point, to try to check for a possible local minimum (case 6 - new baseline). Its seen that there are marginally no mass gains or difference between the solutions with the different starting point. This indicates that no local minimum was found.

5.6. Summary and Discussion of Results

Table 7 summarises all optimisations. It is possible to conclude that these optimisations provide a large mass reduction, between 56% and 44% of the original baseline. As expected, with the increasing number of constraints, the reduction is smaller.

Regarding the possible wingbox failure, a safety factor of 1.5 was used so that all optimisations would have a maximum index of about $\frac{1}{1.5} = 0.67$. Although some optimisations present a failure index below or within this value, others, such as case 5 and 6, do not. This is, again, in a single point of the wingbox and a singularity. Away from it, the average values are lower than 0.67 and respect the 1.5 safety factor.

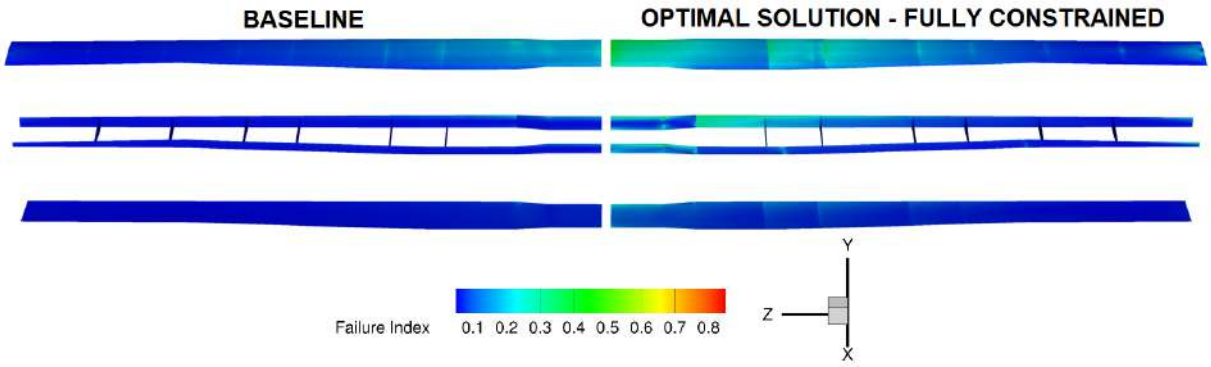

Figure 14: Failure index in initial wingbox (left) and final optimised solution (right)

Table 7: Summary of all optimisation results

Case	Mass difference	Failure index	RAM	Non-dimensional time	Number of iterations	Number of DVs	Number of constraints
Baseline Analysis	REF.	0.47	REF.	1.0	-	-	-
1	−55.6%	0.79	0%	37.8	179	96	26
2	−52.8%	0.67	+2%	61.7	340		27
2 (Different baseline)	−54.4%	0.58	+2%	53.1	286		27
3	−52.5%	0.64	+2%	18.6	134		71
4	−44.6%	0.61	+2%	11.5	71		103
5	−43.9%	0.93	+2%	12.2	75		125
6	−43.6%	0.87	+2%	44.5	142		126
6 (Different baseline)	−43.6%	0.94	+2%	26.1	70		126

In terms of required memory, it is possible to conclude that the effect of the increased number of constraints was very significant and it is mostly from the analysis themselves.

Regarding the computational time, while constraints were being added to the optimisation, from case 1 to 3, the time actually decreased. The reason for that is that the solution is being found in a smaller domain, every time a constraint is added. However, in case 5, the behaviour changed and the time increased again. Although the domain also got smaller, the increased number of constraints require more function evaluations and sensitivities. This means that from case 4 onwards, the computational cost increase by the addition of constraints dominates the decrease in time by having a smaller domain. The only exception is case 6 with a different baseline. Considering that the solution is already close to an optimum, the time it takes is smaller than case 6 with the baseline as starting point. This time changes are associated with number of iterations, scaling up with them.

6. Conclusions and Future Work

Reaching the end of this work, a validated, tested and developed framework for high-fidelity structural analysis and optimisation is provided while also having attained a preliminary optimal solution of the Tekever AR5 wing.

Before reaching this optimal solution, a simpler and detailed model were compared to establish a baseline behaviour and decide which one should be used for the optimisations process. After analysing both, subject to a 4.0g aerodynamic load, the wing revealed to have a safety factor between 2.1 and 3.2 indicating a possible oversized structure and room for improvement. Between both meshes, the detailed model took 9% more CPU time and used 57% more RAM than the simpler mesh. Considering that the time difference scales with the number of optimisations and the memory usage difference is considerable, the simpler mesh was decided as the model to use for the optimisations.

An alternative wingbox structural solution was then obtained after several iterative optimisations, with increasing number of constraints. The final solution led to a mass reduction of 43.6%, while maintaining its structural rigidity, with a 1.5 safety factor and satisfying the necessary manufacturing constraints. It is also important to note that, with further refinement of the computational model in terms of material characterization, with more accurate mechanical properties, this methodology and high-fidelity framework can be a powerful tool to create optimal wing structural solutions.

As future work, the engines' weight and their act-

ing thrust and torque can be included, as well as buckling constraints.

References

[1] Sara Gallardo-Saavedra, Luis Hernández-Callejo, and Oscar Duque-Perez. Technological review of the instrumentation used in aerial thermographic inspection of photovoltaic plants. *Renewable and Sustainable Energy Reviews*, 93:566–579, 2018. doi:10.1016/j.rser.2018.05.027.

[2] Dimosthenis C Tsouros, Stamatia Bibi, and Panagiotis G Sarigiannidis. A review on UAV-based applications for precision agriculture. *Information*, 10(11):349, 2019. doi:10.3390/info10110349.

[3] Huang Yao, Rongjun Qin, and Xiaoyu Chen. Unmanned aerial vehicle for remote sensing applications—a review. *Remote Sensing*, 11(12): 1443, 2019. doi:10.3390/rs11121443.

[4] Pamela Cohn, Alastair Green, Meredith Langstaff, and Melanie Roller. Commercial drones are here: The future of unmanned aerial systems. *McKinsey & Company*, 2017.

[5] Tekever official website - about, Oct 2021. URL `https://www.tekever.com/about/`. Accessed on the 15th of december 2022.

[6] Khodijah Kholish Rumayshah, Aditya Prayoga, and Mochammad Agoes Moelyadi. Design of high altitude long endurance UAV: Structural analysis of composite wing using finite element method. In *Journal of Physics: Series*, volume 1005, page 012025. IOP Publishing, 2018. doi:10.1088/1742-6596/1005/1/012025.

[7] Graeme J Kennedy and Joaquim RRA Martins. A parallel finite-element framework for large-scale gradient-based design optimization of high-performance structures. *Finite Elements in Analysis and Design*, 87:56–73, 2014. doi:10.1016/j.finel.2014.04.011.

[8] Junuthula Narasimha Reddy. *Mechanics of laminated composite plates and shells: theory and analysis*. CRC press, 2003. ISBN 0-5493-1592-1.

[9] Joaquim R. R. A. Martins, Graeme Kennedy, and Gaetan K. Kenway. High aspect ratio wing design: Optimal aerostructural tradeoffs for the next generation of materials. In *52nd Aerospace Sciences Meeting*, National Harbor, Maryland, January 2014. doi:10.2514/6.2014-0596.

[10] Neil Wu, Gaetan Kenway, Charles A. Mader, John Jasa, and Joaquim R. R. A. Martins. pyoptsparse: A python framework for large-scale constrained nonlinear optimization of sparse systems. *Journal of Open Source Software*, 5 (54):2564, 2020. doi:10.21105/joss.02564.

[11] Zhoujie Lyu, Zelu Xu, and Joaquim R.R.A. Martins. Benchmarking optimization algorithms for wing aerodynamic design optimization. In *The 8th International Conference on Computational Fluid Dynamics*, Chengdu, Sichuan, China, July 2014. ICCFD8-2014-0203.

[12] Lin Zhou, Jiangtao Huang, Zhenghong Gao, and Wei Zhang. Three-dimensional aerodynamic/stealth optimization based on adjoint sensitivity analysis for scattering problem. *AIAA Journal*, 58(6):2702–2715, 2020. doi:10.2514/1.J059136.

[13] Guangda Yang and Andrea Da Ronch. Aerodynamic shape optimisation of benchmark problems using su2. In *2018 AIAA/ASCE/AHS/ASC Structures, Structural Dynamics, and Materials Conference*, Kissimmee, Florida, January 2018. doi:10.2514/6.2018-0412.

[14] Isaac Gibert Martínez, Frederico Afonso, Simão Rodrigues, and Fernando Lau. A sequential approach for aerodynamic shape optimization with topology optimization of airfoils. *Mathematical and Computational Applications*, 26(2), 2021. doi:10.3390/mca26020034.

[15] Ahmed El Ibrahim, Sohayb Abdulkerim, and Ibrahim Göv. Aero structural optimization for sailplane wing in preliminary design. *Journal of Advances in Technology and Engineering Research*, 4, 02 2018. doi:10.20474/jater-4.1.5.

[16] Graeme Kennedy and Joaquim R. R. A. Martins. *A Comparison of Metallic and Composite Aircraft Wings Using Aerostructural Design Optimization*. Indianapolis, Indiana, September . doi:10.2514/6.2012-5475.

[17] Gaetan K. W. Kenway and Joaquim R. R. A. Martins. Multipoint high-fidelity aerostructural optimization of a transport aircraft configuration. *Journal of Aircraft*, 51(1):144–160, 2014. doi:10.2514/1.C032150.

[18] N.P.M. Werter and R. De Breuker. A novel dynamic aeroelastic framework for aeroelastic tailoring and structural optimisation. *Composite Structures*, 158:369–386, 2016. doi:10.1016/j.compstruct.2016.09.044.